Chemical Science

ROYAL SOCIETY OF CHEMISTRY

EDGE ARTICLE

View Article Online
View Journal | View Issue

Cite this: *Chem. Sci.*, 2025, **16**, 11347

All publication charges for this article have been paid for by the Royal Society of Chemistry

X-ray fluorescence microscopy and X-ray absorption spectroscopy reveal the stability of the plecstatin-1 scaffold in biological model systems: comparison of Ru, Os and Ir analogues†

James H. Lovett, [a] Barry P. Lai,[b] Hugh O. Bloomfield, [c] Ani T. Baker, [a] Matthew P. Sullivan, [c] Christian G. Hartinger [c] and Hugh H. Harris *[a]

Plecstatin-1 ([RuCl(*p*-cym)(pca)]Cl; *p*-cym = *p*-cymene, pca = (4-fluorophenyl-2-pyridinecarbothioamide)) is an organometallic anticancer compound of the ruthenium "piano-stool"/"half-sandwich" class which displays promising pre-clinical results. Its mode of action is ascribed to targeting plectin in the cytoskeleton to inhibit cancer cell motility. In this research, we report X-ray fluorescence microscopy (XFM) data demonstrating that the cellular distributions of the metals from the Os and Ir analogues of plecstatin-1 are identical to that of Ru in SKOV-3 ovarian cancer cells treated with plecstatin-1. Extended X-ray absorption fine structure (EXAFS) spectroscopy data confirms that both the *p*-cym, and the ancillary pca ligand, remain coordinated after incubation of plecstatin-1 in cell media (in the presence or absence of foetal bovine serum), or, in whole human blood, with the likely ligand substitution of the chlorido ligand for a thiol when available. The apparent stability of the complex scaffold to challenge from a wide variety of biological ligands can be used to rationalise the similar cell targeting behaviour of the Ru, Os and Ir complexes.

Received 22nd April 2025
Accepted 16th May 2025

DOI: 10.1039/d5sc02925b

rsc.li/chemical-science

1 Introduction

Anticancer drug candidates based on a ruthenium (Ru) centre have been rigorously investigated over the last three decades, following the discovery of the antineoplastic and antimetastatic activities of the Ru^{III} compounds known as KP1019 and NAMI-A, respectively.[1–3] More recently, focus has shifted to the organometallic Ru^{II} "half-sandwich" class of compounds.[4–8] Whereas rigorous descriptions of the pharmacokinetics and structure–activity relationships of Ru^{III} compounds remain elusive and ill-defined,[9,10] Ru^{II} anticancer compounds have attracted the bulk of the recent attention owing to the predictability and tunability of their aqueous and physiological properties, facilitating a more predictable route for the rational design of new compounds.[4,11,12] Attention has more recently turned to analogues of these complexes comprising the third row transition metals osmium (Os) and iridium (Ir), with a general trend towards slower aquation kinetics and a longer half-life of the intact compound upon introduction to physiological media.[13–19]

Ru^{II}, Os^{II}, and Ir^{III} are d^6 metal centres that favour low-spin electronic configurations and octahedral geometries. In the motif of an organometallic half-sandwich complex, three of the six available coordination sites are occupied by an η^6-arene (or η^5-cyclopentadienyl anion in the case of Ir^{III}), which stabilises the low oxidation state of the metal centre. The three remaining sites can be occupied by three monodentate ligands, a monodentate and bidentate ligand, or one tridentate ligand.

Most commonly, octahedral Ru^{II} and Os^{II} drug candidate complexes are designed with one or two labile leaving ligands (usually halides), and the complex can be hydrolysed to its aqua form.[20–22] The aquated complex is typically more prone to ligand exchange with biological nucleophiles and intracellular drug targets,[22,23] which might either enhance drug activity or be a mechanism of drug inactivation.[24] In this way, organometallic half-sandwich complexes can be rationally designed as prodrugs, where hydrolysis is suppressed in the high chloride environment of blood ($[Cl^-]$ = 100–160 mM) and then activated by hydrolysis once transported into the low chloride environment within the cytoplasm of the destination cell ($[Cl^-]$ = 4–10 mM).[22]

The remaining coordination sites of the half-sandwich complex can be occupied by ligands of diverse functionalities, which may be tuned to influence the properties of the organometallic anticancer complex. These properties may confer target specificity,[25–27] tune lipophilicity and optimise bioavailability and cell permeability,[28] provide spectroscopic or fluorescent

[a]*Discipline of Chemistry, The University of Adelaide, SA 5024, Australia. E-mail: hugh.harris@adelaide.edu.au*

[b]*X-ray Science Division, Argonne National Laboratory, Lemont, IL 60439, USA*

[c]*School of Chemical Sciences, The University of Auckland, Private Bag 92019, Auckland 1142, New Zealand*

† Electronic supplementary information (ESI) available. See DOI: https://doi.org/10.1039/d5sc02925b

handles for bioimaging and tracking of complex distribution,[29–31] allow tuning of the electronic properties and ligand exchange kinetics of the complex,[32] or facilitate delivery of bioactive ligands that are specifically released upon reaching the drug target as a "payload",[33–35] among many other functionalities that might be imagined or desired.[21,36,37]

Plecstatin-1 (**1**, Fig. 1) is a Ru^{II} half-sandwich organometallic complex featuring η^6-*p*-cymene (*p*-cym) as a π-bound ligand, a labile chlorido leaving ligand, and the bidentate *N*-(4-fluorophenyl)-2-pyridinethiocarbamide (pca) ligand. First reported in 2013, plecstatin-1 was rationally designed to be orally bioavailable owing to the stability of this complex in fairly harsh acidic conditions.[38] Initially, crystal-soaking experiments with the nucleosome core particle (NCP) showed specific binding of plecstatin-1 and the analogous Os complex (**2**, Fig. 1) to histidine residues of the histone proteins and no interactions with DNA.[38] It was later found that plecstatin-1 showed high selectivity for the cytolinker plectin using label-free quantitative shotgun proteomics. The affinity of plecstatin-1 for plectin was enhanced by hydrolysis of the chlorido prodrug to the biologically-active hydroxylated moiety and the necessity of the hydrogen bond-accepting aryl fluoride substituent was established by the substitution of a hydrogen bond-donating hydroxyl, abrogating the selectivity for plectin.[39] Plectin knockout studies have validated the selective binding of plecstatin-1 to plectin *in vitro* by treating keratinocytes isolated from wild-type and plectin-deficient mice.[40] Size-exclusion chromatography-inductively coupled plasma-mass spectrometry (SEC-ICP-MS) has been employed to screen for potential protein binding partners of **1** and **2** in serum obtained from mice bearing CT-26 tumours that were treated with the complexes intraperitoneally and from human serum treated *ex vivo*, indicating that **1** and **2** bound extensively to the blood serum proteins serum albumin and transferrin, with minor fractions bound to immunoglobins and negligible unbound free complex.[41] Further attempts to investigate the interactions of **1** with biomolecules and serum molecules using capillary electrophoresis (CE) have been hindered by the tendency of these samples to aggregate and precipitate after the addition of **1** to the reaction media.[42]

Relative to Ru complexes, Os complexes are typically more inert to hydrolysis (up to 100-fold slower aquation kinetics)[21,43] and form more acidic aqua complexes (*ca.* 1.5 pK_a units lower than Ru complexes).[21,43] In this way, Os complexes are envisaged as prodrugs more persistent in their non-activated, non-hydrolysed form than their isosteric Ru analogues, potentially achieving a longer drug half-life.[44] This is of great interest in organometallic drug design, as isostructural Ru and Os complexes share similar bioactivities and affinities for identical drug targets.[45–47] In the cases where there is a significant deviation in cytotoxicity or bioactivity, this is often attributed to hydrolysis or ligand exchange rate modifications such that these processes no longer occur in a time frame that allows the complex to exhibit these properties.[48,49] The cytotoxicity and pharmacokinetics of a drug might then be tuned by changing the metal centre alone, with minimal disruption to target selectivity or disturbance of the structure–activity relationship.

Distinct from traditional drug design that produced the organic drugs dominant in the pharmaceutical market, where administered forms are typically robust and directly responsible for the mechanism of action, the diverse and often more complex chemistry available to elements in the d-block of the periodic table generates challenges for development and opportunities that may be leveraged for medicinal inorganic chemistry.[50,51] An emerging and exciting facet of metal-based drug design is the area of bioorthogonal catalysis,[52] where unique properties of metal ions, often in organometallic complexes, facilitate highly controlled and specific biochemical outcomes. However, even for this class of metallodrugs, as it is for cytotoxins, including stimuli-responsive examples, an ongoing and crucial requirement is to understand the chemical transformations of the metal complexes within cells (*i.e.* "speciation") so that such information can be included in a closed feedback loop which enables optimisation.[53]

To gain insight into the cellular fates and pharmacokinetics of plecstatin-1 and its Os and Ir analogues (Fig. 1), we have employed synchrotron-based X-ray fluorescence microscopy (XFM) and extended X-ray absorption fine structure (EXAFS) spectroscopy to examine cells, cell growth media and whole human blood treated with these compounds. Synchrotron-based XFM and EXAFS place few restrictions on sample matrices, allowing data on a system to be collected as close to the native, unadulterated state as possible and circumventing harsh chemical and physical sample preparation techniques that might disturb the speciation of transition metals subject to analysis.[54] XFM is a non-destructive elemental mapping technique used to examine elemental localisation at sub-micron resolution for elements with atomic number usually $Z \geq 14$.[55] For XFM, we have employed a paraformaldehyde chemical fixation protocol to prepare adherent SKOV-3 ovarian cancer cells on silicon nitride membranes, as validated by previous published work on human cancer cells treated with the Ru anticancer compounds KP1019 and NAMI-A among other studies of metal uptake in treated cells.[56,57] In doing so, we provide insight into the intracellular accumulation of the metal ions of these putative anticancer complexes.

EXAFS is element-specific and reports on the average local coordination environment of the absorbing element of interest up to ~5 Å and can report bond lengths to a precision of ~0.02 Å.[58,59] In this work, we analyse the Ru K-edge EXAFS to elucidate

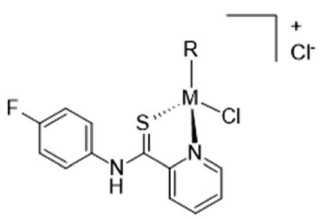

1: M = Ru, R = *p*-cym
2: M = Os, R = *p*-cym
3: M = Ir, R = Cp*

Fig. 1 Structures of plecstatin-1 (**1**), plecstatin–Os (**2**) and plecstatin–Ir (**3**).

the ligand exchange products of plecstatin-1 in cell growth media in the presence or absence of FBS, and in whole human blood. These data and their interpretation then allow us to rationalise the cellular distribution information provided by the XFM analyses.

2 Results and discussion

2.1 Elemental distribution in cells treated with plecstatin-1 and Os and Ir analogues

X-ray fluorescence microscopy (XFM) analysis was conducted on SKOV-3 cells ($n = 5$ in each treatment) treated with plecstatin-1 (Ru) **1**, plecstatin–Os **2** or plecstatin–Ir **3** at the 2-ID-D beamline at the Advanced Photon Source (Argonne National Laboratory, Illinois, USA). Treatment conditions and beamline operating parameters are given in Table 1. Elemental maps were collected from cells treated with **1** using an incident beam energy of 22.7 keV to excite fluorescence from the Ru K-edge while also allowing analysis of the K fluorescence lines of all lighter elements, including the first-row transition metals and all biologically relevant s- and p-block elements. Elemental maps of samples treated with the Os or Ir complexes were collected using an incident beam energy of 13.1 keV to excite the L-edges of these elements while of appropriately high energy to excite K-edge fluorescence of elements with $Z \leq 33$ (Se). Elemental maps of SKOV-3 control cells treated with vehicle alone were collected at 22.7 and 13.1 keV on the same cells (Fig. S2 and S3†).

Table 1 Beamline operating conditions and cell treatment concentrations for the collection of XFM elemental maps for SKOV-3 ovarian cancer cells treated with compounds **1–3**

	Concentration (μM)	Beam energy (keV)	Pixel step size (μm × μm)	Dwell time (ms)
1	20	22.7	0.75 × 0.75	500
2	20	13.1	0.50 × 0.50	150
3	30	13.1	0.50 × 0.50	250

Fig. 2 shows XFM elemental maps of P, Zn and either Ru, Os or Ir from a representative cell treated with either plecstatin-1 **1**, plecstatin–Os **2** or plecstatin–Ir **3**, respectively (see also Fig. S4–S6† for further cell images). The distributions of P and Zn are assumed to correlate with the nucleus of the cell due to the elevated content of these elements. The distribution of Ru in cells treated with **1** appears approximately perinuclear, with its highest concentration in the periphery of the nuclear region. The pixel resolution of cells treated with **1** makes identifying fine structure or organelle localisation of the elements difficult.

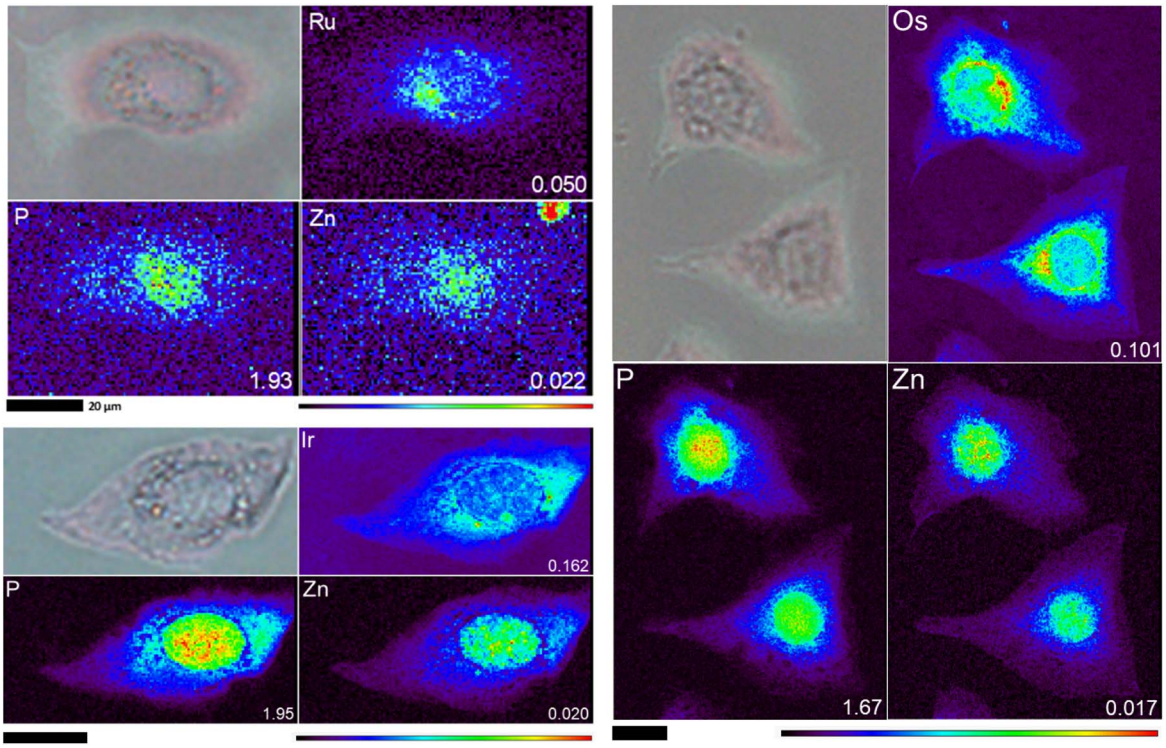

Fig. 2 Elemental maps of P, Zn and the metal of interest (Ru, Os or Ir) collected by XFM on SKOV-3 ovarian cancer cells treated with **1** (20 μM, top left), **2** (20 μM, right) or **3** (30 μM, bottom left). Elemental maps were recorded using a beam energy of 22.7 keV, a beam spot size of 0.75 × 0.75 μm and a dwell time of 500 ms (**1**) or a beam energy of 13.1 keV, beam spot size of 0.50 × 0.50 μm and a dwell time of 150 ms (**2**) or 250 ms (**3**). The maximum pixel intensity is reported for each elemental map in units of areal density (μg cm^{-2}). All scale bars are 20 μm. XFM elemental maps were recorded at the 2-ID-D beamline of the Advanced Photon Source (Argonne National Laboratory, USA). Cells were fixed to silicon nitride windows using a paraformaldehyde fixing protocol (*vide infra*) and cells were selected for elemental mapping by inspection with optical microscopy (top left panel of sample) prior to measurement.

The elemental maps of samples treated with either **2** or **3** were measured using a lower incident beam energy and smaller pixel step-size, and show excellent spatial resolution. Os (**2**) and Ir (**3**) concentrations are highest in the region directly surrounding the nucleus. In the case of cells treated with **3**, clear co-localisation can be seen with the distribution of Ir and the non-nuclear fraction of Zn and P. This pattern of metal distribution may indicate some degree of organelle-specific localisation in the endoplasmic reticulum or mitochondria. The apparent similarity of the elemental maps of cells treated with all three complexes suggests that these complexes exert their cytotoxic activity *via* a similar mechanism, or at the least, show no specific intracellular localisation that might suggest a different mechanism of action or handling of these compounds by the cell.

Although there appears to be some overlap of metal distribution with the nucleus of these cells, because XFM elemental maps are necessarily two-dimensional projections of an object with *z*-axis depth, it is not possible to quantitatively ascertain the nuclear-associated fraction of these complexes using XFM alone. In any case, the distributions of all three of these metals are consistent with previous results that suggest that the target of plecstatin-1 is plectin and the cytoskeletal structure of the cell.[40]

The average intracellular content of Ru, Os, and Ir (Table 2), the biologically-relevant non-metals (P, S and Cl) and metals with $Z > 16$ (K, Ca, Mn, Fe, Cu and Zn) (Table S1†) was assessed for all treated samples and non-treated control cell groups, along with cell areas. Average intracellular elemental content is reported as fg per cell with sample size $n = 5$ for all treatment and control groups, with the uncertainty recorded as the standard error of the mean. An apparent decrease in the area of cells treated with **3** relative to either control, or cells treated with **2**, was not statistically significant (Fig. S7 and Table S1†).

We have previously reported unexpected changes in levels of endogenous elements and morphology of cells after treatment with metal complexes. In particular, we have noted the approximate two-fold increase in intracellular Cu and its co-localisation with Ru in cells treated with 50 μM of Ru265, an inhibitor of the mitochondrial calcium uniporter which localises specifically in mitochondria.[60] It is likely that treating cells with biologically active transition metal complexes might influence redox homeostasis and instigate a corresponding intracellular response and differential (mis)handling of endogenous elements by the cell under stress. Previous work from our group has noted partial co-localisation of Fe with Ru in SH-SY5Y cells treated with 200 μM of the anticancer Ru^{III} complex KP1019, in which the Fe distribution was altered in treated cells relative to control cells, whereas the distribution of other endogenous elements remained unperturbed.[61] In this context, it appears notable that plecstatin-1 and its analogues leave the endogenous metallome unperturbed, with no apparent disruption to the concentration or distribution of the endogenous trace elements Mn, Fe, Cu or Zn as measured by XFM. It may be inferred that these compounds are unlikely to exert a cytotoxic mode of action through redox cycling and the generation of ROS, with the caveat that standard XFM analysis does not report the oxidation status of the elements under analysis. These findings are consistent with the previously proposed hypothesis that the predominant mode of action of plecstatin-1 is through interaction with plectin and subsequent disruption of cellular structure, adherence and motility, providing evidence that, likely, the Os and Ir analogues of plecstatin-1 do not deviate significantly from this principal mode of action.

We note that interesting results have been published using nano-focussed X-ray absorption near-edge structure (XANES) spectroscopy to report the oxidation status of Os in single cells treated with a cytotoxic organoosmium(II) half-sandwich complex that purportedly exerts its anticancer activity *via* intracellular redox cycling.[62] While these results show the utility and promise of nano-focussed XANES to report speciation and localisation information in intact single cells simultaneously, we note the caveats given by the authors in their manuscript. Namely, the pharmacologically relevant concentrations of metal complexes are much too low to provide sufficient fluorescent signal for XANES analysis, except in cases of significant bio-concentration in specific organelles (*e.g.* mitochondria). As the intracellular redox stability of **1** has previously been established and its intracellular localisation and site of action has been previously ascertained to be the cytoskeleton and not localised in organelles, it was suitable to investigate the speciation of this complex using bulk XAS in whole physiological systems.

Table 2 Average intracellular mass content (fg per cell) of Ru, Os or Ir in SKOV-3 ovarian cancer cells treated with compounds **1–3** (cell $n = 5$) derived from XFM measurements. The uncertainty of the elemental mass quantity is given as the standard error of the mean. We note minor crosstalk interference of the Os and Ir XRF signals in this data, likely arising from overlap of nearly coincident L-edge X-ray fluorescence lines of these two elements

	Average intracellular metal mass content (fg per cell)		
	Ru	Os	Ir
1	152 ± 4	—	—
2	—	171 ± 12	38 ± 4
3	—	27 ± 3	489 ± 69

2.2 Speciation analysis in a media surrogate of the biological environment

Extended X-ray absorption fine structure (EXAFS) data were collected from **1** diluted in cellulose or dissolved in 10% DMSO/saline (1 mM). Data were also collected for **1** incubated in cell media in either the presence or absence of 10% foetal bovine serum (FBS) and in human whole blood treated with **1** (100 μM). EXAFS analysis allows for the elucidation of the local coordination environment around the absorbing element of interest. EXAFS is suited to analysing the speciation of heavy elements in complex biological sample matrices as it collects data on only the element of interest, requires minimal sample preparation that may induce changes to the native speciation of the sample *via* harsh chemical or physical methods, and has no theoretical

restrictions on the physical state of the sample analysed (*e.g.* no necessity for crystallinity, absence of particles and debris).

Fig. 3 shows the Ru K-edge EXAFS ($\chi(k)$, k^3-weighted) spectra collected at the XAS beamline of the Australian Synchrotron and analysed using the XAS data analysis software package EXAFSPAK. Structural parameters of the absorber-backscatter distances derived from single-scattering fits to the experimental spectra are given in Table 3.

From the curve-fitting analysis of the EXAFS spectra collected from the samples incubated in media (either with or without FBS) and in human whole blood, it is apparent that both the η^6-*p*-cymene and the bidentate *N*-phenyl-2-pyridinecarbothioamide ligand remain coordinated to the Ru centre. The donor atom on the final coordination site on the Ru centre, occupied by the chlorido ligand in the parent complex, cannot be definitively assigned as either S or Cl in our analyses of these samples. The phase and amplitude components of an EXAFS signal from a backscattering atom with a constant absorber atom is primarily governed by the absorption cross-section of the backscattering atom, proportional to the size and density of the electron distribution around that atom. Therefore, distinguishing the identity of one backscattering atom from another of similar atomic number (*i.e.* S and Cl) is an almost impossible task in practice. However, EXAFS analysis can definitively distinguish between backscatterers of significantly different atomic number, *e.g.* between N or O and S or between S and Se.

Crystallography data published on plecstatin-1 from crystal-soaking experiments revealed Ru binding to two different histidine residues of the H2B subdomain of the NCP.[38] These data revealed cleavage of the pca ligand, leaving the Ru(*p*-cym) moiety bound to His, although the parallel experiment using the Os analogue **2** suggested that both ligands remain bound to the metal centre for this species. Similar crystal-soaking experiments using the Ru(*p*-cym) anticancer complexes RAPTA-C and RAED-C showed binding to histidine residues of

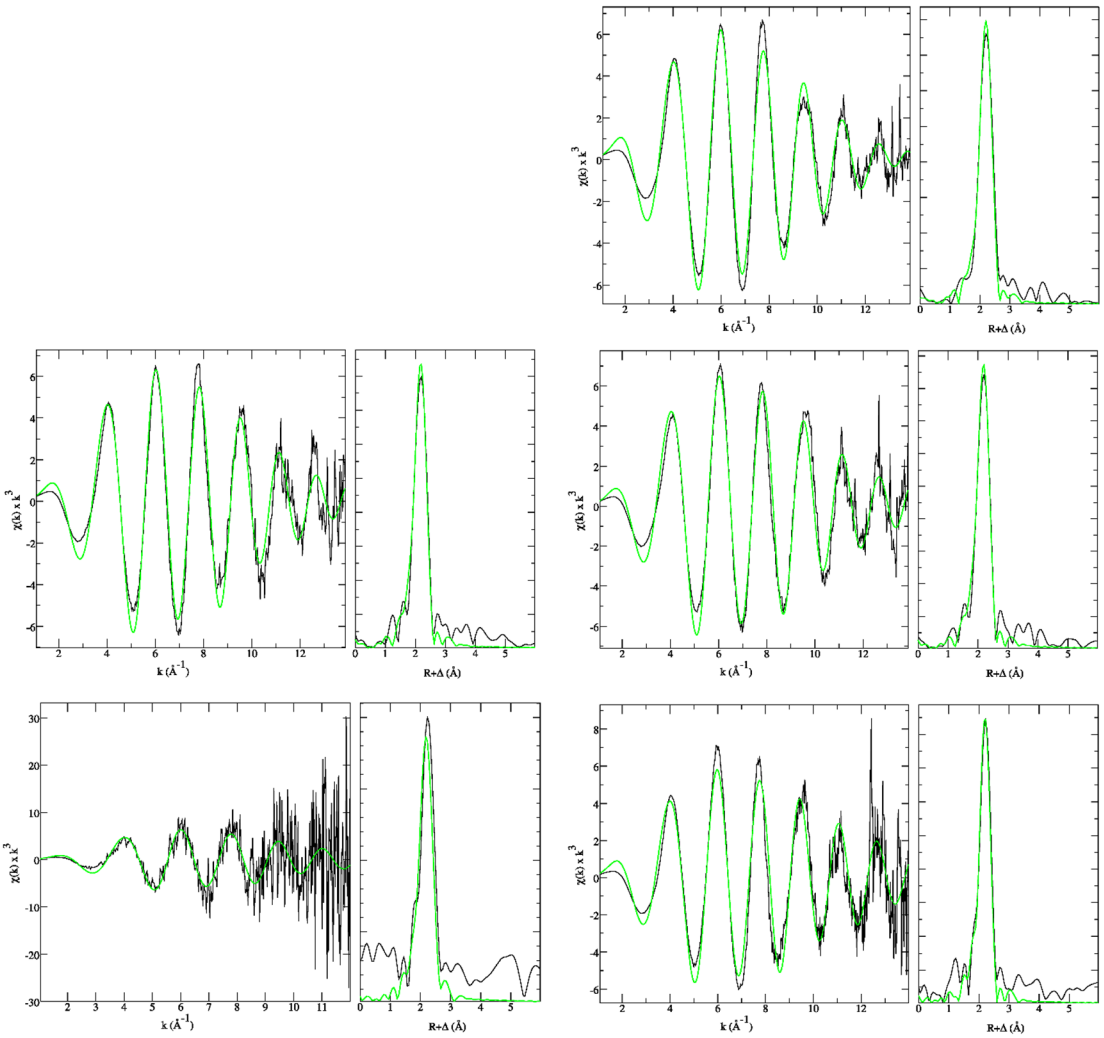

Fig. 3 Raw data (black) and model spectra generated using FEFF8 (green) of the EXAFS $\chi(k)$ (left) and the Fourier transform (right) spectra analysed using a single-scattering model within the analysis software suite EXAFSPAK. Data presented are of **1** ground in cellulose (top right), **1** (1 mM) incubated in DMEM/F12 media in the absence (middle left) or presence (middle right) of 10% FBS (1 mM, 10% DMSO), **1** (0.1 mM) incubated in human whole blood (37 °C, 1 h; bottom left) and **1** (1 mM) dissolved in 10% DMSO/saline (bottom right).

Table 3 Structural parameters of **1** (plecstatin-1) derived from EXAFS fitting calculations. EXAFS curve-fitting analysis was performed using the software package EXAFSPAK and the *ab initio* fitting code FEFF8[a]

	Path	R (Å)	σ^2 ($\times 10^3$ Å^2)	ΔE_0 (eV)
Best fit [7 × Ru–C/N ($Z = 6$), 2 × Ru–S/Cl ($Z = 16$)]				
Cellulose ($F = 0.234$)	Ru–C/N	2.190(1)	3.5(1)	−10.8(2)
	Ru–S/Cl	2.391(1)	2.4(1)	
Media ($F = 0.286$)	Ru–C/N	2.168(4)	3.7(3)	−13.2(6)
	Ru–S/Cl	2.361(4)	2.0(2)	
Media + FBS ($F = 0.262$)	Ru–C/N	2.166(4)	3.4(3)	−13.3(6)
	Ru–S/Cl	2.360(3)	1.5(2)	
Whole blood ($F = 0.898$)	Ru–C/N	2.167(26)	3.8(2.3)	−13.1(4.3)
	Ru–S/Cl	2.374(25)	1.0(0.9)	
DMSO/saline ($F = 0.431$)	Ru–C/N	2.215(6)	4.4(5)	−11.1(9)
	Ru–S/Cl	2.366(6)	3.5(4)	
Alternative model [8 × Ru–C/N/O ($Z = 6$), 1 × Ru–S/Cl ($Z = 16$)]				
Media ($F = 0.302$)	Ru–C/N/O	2.193(3)	3.5(3)	−10.3(6)
	Ru–S/Cl	2.379(5)	0.6[b]	
Media + FBS ($F = 0.283$)	Ru–C/N/O	2.192(3)	3.4(3)	−10.4(6)
	Ru–S/Cl	2.375(5)	0.5[b]	
Whole blood ($F = 0.902$)	Ru–C/N/O	2.204(19)	3.6(2.3)	−9.4(3.7)
	Ru–S/Cl	2.392(36)	0.1[b]	
DMSO/saline ($F = 0.439$)	Ru–C/N/O	2.220(4)	3.2(3)	−9.0(7)
	Ru–S/Cl	2.392(7)	1.1(4)	

[a] The k-range was 1.1–13.9 Å^{-1} and a scale factor ($S_0{}^2$) of 0.9 was used for all fits except for the whole blood sample, which used a k-range of 1.1–11.9 Å^{-1}. $\Delta E_0 = E_0 - 22.135$ (keV), where E_0 is the threshold energy. Values in parentheses are the estimated standard deviation derived from the diagonal elements of the covariance matrix and are a measure of precision. The fit-error (F) is defined as $[\Sigma k^6(\chi_{exp} - \chi_{calc})^2/\Sigma k^6 \chi_{exp}{}^2]^{1/2}$. [b] These values of σ^2 are already too low ($\ll 1 \times 10^{-3}$ Å^2) to be considered physically realistic. Further refinements of this parameter converged to negative values to satisfy the curve-fitting algorithm, resulting in our abandonment of this model as a viable structure.

the H2B subdomain of the NCP.[63] However, our attempts to fit the EXAFS spectrum of **1** in media (with or without FBS) or whole blood by replacing one Ru–S/Cl scattering path with a Ru–N path led to physically unreasonable fit parameters. The magnitude of the Debye–Waller factor (σ^2) of the Ru–S/Cl component in this structural model optimised to negative values as the curve-fitting algorithm attempted to compensate for the halving of the backscatterer coordination number. For this reason, a structural model featuring only one heavy S/Cl backscatterer was eliminated as a viable fit candidate, and we ruled out histidine or another N-donating ligand as a nucleophile that could effectively compete with cysteine or another S-donating ligand for coordination to **1** in this system.

Coordination of both a chlorido and a sulfur donor ligand in the first coordination shell of Ru was used as the initial structural model for EXAFS curve-fitting for all samples, using atomic coordinates obtained from the crystal structure previously published by Meier *et al.*[38] The assignment of coordination number (formally scattering path degeneracy, N) to the Cl and S scattering paths was challenging due to both the intrinsic difficulty of distinguishing between two elements with very similar atomic number and the very similar XRD bond lengths of Ru–S (2.367 Å) and Ru–Cl (2.369 Å) (accuracy of bond length determined by EXAFS is typically $\Delta R = \pm 0.02$ Å). Assessment of different structural models for single-scattering and multiple-scattering fits failed to resolve either the Ru–C/N or Ru–S/Cl paths into discrete EXAFS backscattering components while maintaining stability of the final parameters and physically sensible bond lengths and Debye–Waller factors. The best fit across all three datasets was achieved using only two components; one path for Ru–C/N backscattering atoms ($N = 7$, $Z = 6$) and one path for Ru–S/Cl ($N = 2$, $Z = 16$).

The amplitude of a scattering path contributing to the EXAFS signal is proportional to both $S_0{}^2$ and N and inversely proportional to kR^2, where $S_0{}^2$ is the amplitude reduction factor. $S_0{}^2$ is related to the intrinsic losses in the yield of ejected photoelectrons returning in phase to the absorbing atom, *e.g.* by relaxation of the finite lifetime core-hole of the excited state absorbing atom or by inelastic scattering of the photoelectron. In practice, it is not possible to determine $S_0{}^2$ during an XAS experiment and it is generally estimated in the fitting model as a constant between 0.7 and 1.0 (although there is some evidence that $S_0{}^2$ is weakly energy-dependent);[64] for $S_0{}^2$ a value of 0.9 was chosen in all models presented in this work. A corollary to not being able to explicitly determine $S_0{}^2$ is that it introduces uncertainty in determining N, typically on the order of 20–25%.[64]

Choosing $N = 0$, 1, or 2 for S and Cl (such that $N(S) + N(Cl) = 2$) for separate scattering shells never yielded chemically-reasonable fit parameters; the Debye–Waller factor (σ^2) of one path would increase to an infeasibly high value ($>7.00 \times 10^{-3}$ Å^2) while the other would simultaneously converge to an infeasibly low or even negative value. To circumvent this, we eliminated the Ru–Cl scattering path and modelled the Ru–S/Cl paths as a single $N = 2$ Ru–S component. A similar analysis led to modelling of the Ru–C and Ru–N paths, which have very similar bond lengths in

the reported related crystal structures, as one Ru–C component with $N = 7$.

The mode of action of Ru^{II} organometallic anticancer compounds, and halido-coordinated anticancer organometallics more generally, is rationally designed around the hydrolysis of the halido ligand followed by subsequent binding to macromolecules, often *via* reduced thiolate groups. Plecstatin-1 is likely bound to a thiolato ligand in serum-containing media, however, the unambiguous identity of biomolecular ligands cannot be confirmed using XAS alone. Our group has previously investigated the aqueous stability of Ru half-sandwich complexes and their interactions with serum proteins using capillary electrophoresis (CE) and hyphenated mass spectrometry (MS) techniques. Human serum albumin (HSA) and transferrin (Tf) were shown to interact with organoruthenium complexes, including **1**, and Ru-complex interactions were also assessed in simulated media, cell culture medium and human serum to evaluate hypothetical protein binding partners for these complexes in physiologically relevant systems. Although these methods yielded interesting results for a hydroxyquinoline-derived complex, incubation of **1** in all sample matrices induced precipitation that occluded the identification of any protein binding partners in these experiments.[42] In this previous report, precipitation likely resulted from an experimental requirement to dilute reaction mixtures in 20 mM phosphate buffer; note that in the current work, the XAS samples were not diluted in this manner, and no precipitation was observed.

With the identity of any potential biomolecular binding partner not yet being explicitly elucidated, we present here that any candidate should feature a sulfur-donating ligand as opposed to a hard Lewis base donor, concomitant with the EXAFS results of **1** incubated in media and whole blood.

The EXAFS spectrum of **1** dissolved in 10% DMSO/saline was the only sample that yielded physically-reasonable fit parameters for the alternative fitting model of 8 × Ru–C/N/O, 1 × Ru–S/Cl. This seemed curious at first, as it represented a model of hydrolysed **1** in a solution with high concentrations of chloride and DMSO. As such, different fractions of N for each component were tested and refined by floating N followed by floating all other structural parameters in unison. The results of each refinement returned almost equal goodness-of-fit (F) values with no obvious "red flags" in the structural parameters R, σ^2 or ΔE_0. However, upon further refinements the fit consistently converged on the 7 × Ru–C/N, 2 × Ru–S/Cl model and in the absence of any evidence for hydrolysis in this sample, this was accepted as the best fit. The bond length of the Ru–S/Cl component in the best fit is comparable to the samples first dissolved in DMSO and added to biological media, and shorter than R for the same component in the cellulose standard, which retains the chlorido ligand and appears to indicate the substitution of chloride for a shorter Ru–S bond.

Previously reported crystal structures of **1** showed only an *N*,*S*-coordination mode of the pca ligand to the metal centre. However, amido-switching has been observed in **2**, leading to *N*,*N*-coordination to the metal centre.[38] Furthermore, plecstatin-1 can dimerise in aqueous solution, with two thione bridges between the two Ru constituents of the dimer. Dimerisation was reported to persist in the presence of sulfur-containing amino acids, however, was abrogated by the use of DMSO to prepare stock solutions.[38] EXAFS curve-fitting of structural models to plecstatin-1 data in the present work confirms the *N*,*S*-coordination mode of pca first observed by X-ray diffraction analysis. Sulfur has a much larger backscattering cross-section than nitrogen, corresponding to a much greater scattering amplitude from sulfur in the coordination sphere, relative to nitrogen. Furthermore, the Ru–S bond is typically much longer than the Ru–N bond due to coulombic and orbital overlap effects, and significantly greater in length than the limit of bond length resolutions in an EXAFS experiment ($\Delta R \approx 2\pi/\Delta k \approx \pm 0.02$ Å). Structural models for the EXAFS data incorporating the light backscattering atoms N or O substituting for S or Cl were rejected due to poor or unstable fits, indicating that no amide switching was observed under the conditions investigated and that plecstatin-1 remains intact as-synthesised in cell media in either the presence or absence of biological reductants. No evidence of dimerisation was observed, which would be apparent through the presence of a Ru–Ru peak at ~3.6 Å in the EXAFS Fourier transformation. This is consistent with dissolution of **1** in DMSO inhibiting dimerisation. If **1** had undergone rapid aquation of the chlorido ligand in water, then the hydrolysis step would facilitate the subsequent ligand exchange for a thiol-containing biomolecule. However, the XAS experiments gave strikingly similar spectra for **1** incubated in media in either the presence or absence of FBS (Fig. S9†), which provides the vast majority of nucleophilic thiols to the media. We propose that the "second" sulfur donor ligand in the coordination sphere of **1** in media in the absence of FBS is derived from solvent DMSO during the preparation of the stock solution before incubation in media. This proposed mechanism is

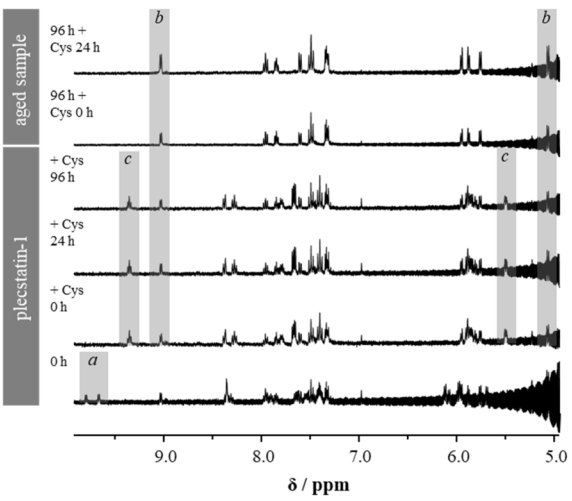

Fig. 4 ^{1}H NMR spectra (400 MHz, D_2O) of plecstatin-1 (2 mM, species *a*) with and without L-cysteine (1 mol eq.) incubated for 96 h. To the latter sample, Cys was added and the reaction was remeasured after 24 h. Plecstatin-1 (*a*) dimerises in aqueous solution to form *b*, which is stable upon addition of Cys. Once formed, the dimer does not react with Cys, while plecstatin-1 forms a Cys adduct (species *c*).

further supported by considering the magnitudes of ΔE_0 for the three samples. A shift of ΔE_0 to more negative energies, as observed for the −2 eV shift of both media samples relative to the cellulose pellet, is an unsurprising result for the exchange of a chlorido ligand for a less electronegative sulfur-donor ligand. The formation of the **1**–DMSO adduct effectively "blocks" the formation of the plecstatin-1 dimer, however, it is likely readily exchanged for a nucleophilic thiol from a biological reductant such as those that would be abundant in FBS. Indeed, the inhibition of dimerisation by an S-donor ligand was observed in the reaction of plecstatin-1 with L-cysteine (Cys) in D_2O, which we investigated by ^{1}H NMR spectroscopy. When the compound was dissolved in D_2O, signal sets assignable to monometallic (Fig. 4, species *a*) and dimerised species (Fig. 4, species *b*) were observed, presumably with the pca sulfur atoms acting as bridging ligands. After 96 h of incubation, the compound was completely converted into the dimeric form. When Cys was added to plecstatin-1 in D_2O at a 1 : 1 molar ratio, the first spectrum recorded immediately after mixing had already significantly changed compared to that obtained for pure plecstatin-1. While the peaks assigned to the dimeric species were visible, the monomer immediately converted into the Cys adduct (Fig. 4, species *c*), most prominently evidenced by a significant upfield shift of the proton neighbouring the pyridyl nitrogen atom. Over the course of 96 h, the spectra did not change significantly, indicating that Cys did not affect the dimer once established in aqueous solution. This observation was confirmed by the addition of Cys to a sample of plecstatin-1 in D_2O that was aged for 96 h. In this case, only peaks assignable to the dimeric form were observed, and the spectrum recorded after a 24 h-incubation period was virtually identical, supporting the high stability of the dimer once established. These studies confirm that Cys binding to plecstatin-1 prevents it from dimerising in solution, supporting the EXAFS data, which did not indicate the presence of dimer. As the EXAFS sample contained chloride, dimerisation would have been prevented or slowed down significantly, which explains the lack of a signal assignable to a dimer under these conditions and the detection of the S(/Cl)-coordinated adduct.

3 Materials and methods

Compounds **1–3** were synthesised according to literature methods.[38] Compounds were stored away from light at room temperature before cell treatments. After the cells were treated with the compound, they were fixed to silicon nitride membranes and transported to the Advanced Photon Source (APS; Argonne National Laboratory, USA). Plecstatin-1 cellulose pellet standard and media samples were prepared on-site at the Australian Synchrotron (AS; Clayton, Australia).

3.1 X-ray fluorescence microscopy

3.1.1 Cell culture. Silicon nitride membranes (Silson Ltd, Warwickshire, England) were washed sequentially for 2 min each in Milli-Q water, 70% ethanol, and 100% ethanol in a small Petri dish. The membranes were air-dried under sterile conditions and transferred into wells of 12-well culture plates, which had been previously exposed to UV-light overnight.

SKOV-3 cells were kindly provided by Dr Carmela Ricciardelli from the Robinson Research Institute at The University of Adelaide, Australia. The cells were cultured in a T75 flask and collected after trypsinisation (0.25% trypsin and ethylenediaminetetraacetic acid) for 3 min. The cells were spun down at 1200 rpm for 5 min. Cell supernatant was discarded and the pellet was suspended in 1 mL culturing media (DMEM/F12, 10% FBS, L-glutamine, 1% penicillin/streptomycin and 0.1% Fungizone).

Cell suspensions were mixed with trypan blue solution (0.4%) and transferred into a cell counting chamber slide (Thermo Fisher Scientific Australia, Adelaide, Australia). The viable cells were counted with Countess II (Thermo Fisher Scientific Australia, Adelaide, Australia). The cell suspensions were prepared with culturing media and ∼2000 SKOV-3 cells were seeded onto each membrane without contacting the pipette tip. The cells were incubated for 3 h at 37 °C and 5% CO_2 atmosphere for attachment. Culturing media (1.4 mL) was added carefully to each well and the cells were incubated overnight at 37 °C, 5% CO_2.

3.1.2 Metal complex incubation and cell fixation. Cells adhered to the silicon nitride membranes were treated with **1** (20 μM, 1% DMSO in media), **2** (20 μM, 1% DMSO in media) or **3** (30 μM, 1% DMSO in media) in 2 separate portions of 0.7 mL, enough to soak the cell-coated silicon nitride membrane in solution. The cells were incubated in the media containing the respective compound for 4 h (37 °C, 5% CO_2). The treatment solution was aspirated from the well carefully, avoiding contact with the membrane, and then the membrane was washed with PBS (0.7 mL) and then aspirated. The cells were fixed onto the membrane with 4% paraformaldehyde in PBS (0.7 mL). After 5 min, the paraformaldehyde solution was aspirated. The membrane was washed twice with PBS (0.7 mL) for 5 min each, twice with a solution of trace metal-free ammonium acetate (100 mM, 0.7 mL) for 2 min each and finally with Milli-Q water (0.7 mL) to cover the surface of the membrane and to wash out excess ammonium acetate. Milli-Q water was removed immediately by blotting with tissue and the membrane was then allowed to dry completely while protected from dust. The membrane was stored in a sealed plastic vessel at room temperature for subsequent analysis.

3.1.3 Advanced Photon Source beamline operating conditions. Elemental distribution maps of SKOV-3 cells treated with **1**, **2** or **3** were measured at the 2-ID-D beamline at the Advanced Photon Source (Argonne National Laboratory, Lemont, IL) with modifications to the protocol described previously.[60] The beamline used a double multilayer monochromator and a gold "high flux" zone plate setup to focus a monochromatic beam into a spot of 300–400 nm full width at half maximum (FWHM) in diameter. The same Fresnel zone plate arrangement was used to focus the X-ray beam to the same spot size at the lower energy setting. An energy-dispersive silicon drift detector (Vortex EM, SII Nanotechnology, Northridge, CA, USA) was used to collect the X-ray fluorescence spectra from the sample, which was placed in a He environment at 75° to the incident beam. All

elemental maps were recorded in fly-scan mode. Elemental maps were generated with the MAPS software package[65] by Gaussian fitting of the raw emission spectra for each image pixel. The Gaussian peaks were matched to characteristic X-ray emission lines to determine the fluorescence signal for each element. Quantification of the data (in $\mu g\ cm^{-2}$) was performed by comparing the X-ray fluorescence intensity to those from National Bureau of Standards thin film standards NBS-1832 and NBS-1833 (National Bureau of Standards, Gaithersburg, MD, USA) measured at the same position as the sample measurements.

Elemental maps of SKOV-3 cells treated with **1** were collected with an incident beam energy of 22.7 keV to excite the K-edge fluorescence of Ru and all lighter elements. The pixel step size of these maps was 0.75 μm × 0.75 μm and the per pixel dwell time was 500 ms. Elemental maps of cells treated with either **2** or **3** were recorded at 13.1 keV to excite the L-edge fluorescence of these third-row transition metals simultaneously with the K-edge fluorescence of all first-row transition metals and lighter elements. The pixel step size of all elemental maps recorded for cells treated with **2** or **3** was 0.50 μm × 0.50 μm. The per pixel beam dwell time was 150 ms for all cells treated with **2** and 250 ms for all cells treated with **3**. Elemental maps of untreated control cells were taken at the higher and lower energy settings on the same set of cells. The pixel step size was 0.75 μm × 0.75 μm and the dwell time was 500 ms when the control cells were measured at 22.7 keV and 0.50 μm × 0.50 μm and 200 ms when measured at 13.1 keV.

3.1.4 Data analysis. Region-of-interest (ROI) analysis of the cells was conducted by drawing ROIs around a particular cell using the ROI analysis tool in the XFM data analysis software MAPS.[65] Intracellular elemental quantitation was achieved in MAPS by per-pixel spectrum fitting of the samples, followed by integration of the entire elemental concentration in the ROI to give elemental quantities in mass units (fg per cell). Statistically significant variations in the mean of cell areas and intracellular elemental concentrations between samples were calculated using ANOVA in the GraphPad Prism software suite. Statistically significant variations between samples in the means of cell areas and intracellular elemental content were calculated using the GraphPad Prism software suite. An unpaired, two-tailed Student's *t*-test with Welch's correction was used to determine the *p*-value for the difference in mean intracellular ruthenium concentration of samples treated with plecstatin-1 and untreated control cells, both measured at 22.7 keV. The cell areas of samples and the intracellular elemental content of all other elements measured were analysed by one-way ANOVA tests, and the mean of each sample group was compared against the mean of each of the other groups using Dunnett's T3 multiple comparisons test. The large and significant differences in the means of cell areas and intracellular content of several elements between control cells measured at 13.1 keV and 22.7 keV confirmed there was no validity in comparing between samples measured at different energies, and all comparisons between treatment groups measured at different energies have been ignored.

3.2 X-ray absorption spectroscopy

3.2.1 Cellulose pellet standard. 1 was ground with cellulose in a mortar and pestle to achieve sufficient dilution of the overall Ru concentration and an optimal fluorescence signal to collect EXAFS data in fluorescence mode at the XAS beamline. The pressed cellulose pellet was transferred to a plastic sample cuvette holder covered with Kapton tape and analysed within 1 h of preparation.

3.2.2 Media samples. 1 was dissolved in DMSO before dilution in DMEM/F12 media in the presence or absence of 10% FBS (10% final DMSO concentration). Media solutions (100 μL) were injected into a plastic sample cuvette holder covered with Kapton tape and immediately flash-frozen in liquid nitrogen (LN_2). The frozen media samples were immediately placed in the beamline for XAS analysis. All media samples were analysed within 1 h of preparation.

3.2.3 Human whole blood sample. Blood was collected with informed consent from a volunteer and experiments were conducted with protocols and conditions approved by the University of Adelaide Human Research Ethics Committee (approval number H-2024-155). Human whole blood was collected into heparinised vacutainers and stored on ice before usage (1 h). Physiological saline was prepared by dissolution of sodium chloride in Milli-Q ultrapure water for a final concentration of 160 mM. **1** was dissolved in DMSO before dilution in physiological saline and pH was adjusted to 7.4 with aqueous sodium hydroxide (1 M) for a final concentration of 1 mM (10% DMSO). Whole blood (900 μL) and **1** treatment solution were preheated to 37 °C before the addition of the treatment solution to the blood (100 μM, 1% DMSO). After 1 h, the blood reaction mixture (100 μL) and the DMSO/saline solution (100 μL) were injected separately into plastic sample cuvette holders covered with Kapton tape and immediately flash-frozen in LN_2. The frozen samples were stored on LN_2 before analysis at the beamline.

3.2.4 EXAFS data collection and analysis. Ru K-edge X-ray absorption spectra were recorded on the X-ray absorption spectroscopy (XAS) beamline at the Australian Synchrotron (Clayton, Australia). The energy of the electron beam was 3.0 GeV with a current of ~200 mA. The incident X-ray beam was sourced from a wiggler insertion device and the requested beam energy was selected by employing a Si(111) double crystal monochromator with rejection of higher order harmonics achieved using a rhodium-coated mirror. Samples were measured in fluorescence mode and fluorescence data were collected for cellulose and media samples by a 100-element germanium detector (Canberra/UniSys) oriented at 90° to the incident beam to minimise background noise from scattered photons. Whole blood and DMSO/saline samples were measured in fluorescence mode by an 18-element germanium detector (Mirion, France) oriented at 90° to the incident beam. During data collection, the samples were maintained at a temperature of ~10 K using a helium pulsed expansion cooled cryostat (Cryo Industries, Manchester, NH, USA). The spectrum of a Ru foil, recorded in transmission downstream from the sample, was used as an internal standard to calibrate the energy

scale for the first peak of the first derivative of the elemental Ru K-edge (22.118 keV).

3.2.5 Data analysis. Calibration, averaging and background subtraction of all spectra were performed using the EXAFSPAK software package (G. N. George, SSRL), available at **https://www-ssrl.slac.stanford.edu/~george/exafspak/exafs.htm**. Phase and amplitude functions for single scattering electron paths were generated by the *ab initio* code FEFF8,[66] and these paths were fit to the experimental data using EXAFSPAK.

3.3 NMR spectroscopy

Plecstatin-1 (2 mM) and L-cysteine (1 mol eq.) were combined in D_2O and ^1H NMR spectra were recorded immediately and after 24 and 96 h. Additionally, a solution of plecstatin-1 (2 mM) in D_2O was incubated for 96 h before the addition of L-cysteine (1 mol eq.), after which ^1H NMR spectra were measured immediately and after 24 h.

4 Conclusions

The mode of action of organometallic anticancer agents is difficult to decipher, and there are only a few compounds for which the molecular targets have been identified and validated. Plecstatin-1 is one of these compounds, and it was shown to target the scaffold protein plectin. Elemental maps generated by X-ray fluorescence microscopy revealed that the Ru distribution in SKOV-3 ovarian cells treated with plecstatin-1 was consistent with the selectivity for plectin in the cytoskeleton of cancer cells. To elucidate the role of the metal centre in plecstatin-1, elemental maps of cells treated with the Os and Ir analogues of plecstatin-1 were recorded. These revealed similar distribution patterns as those observed for cells treated with the Ru complex, indicating that the Os and Ir complexes likely exert their cytotoxic action in the same manner as plecstatin-1 and that the primary mechanism of action of this class of compounds is independent of the choice of metal centre. As the metal centres are known to have very different ligand exchange kinetics, this impacts the interaction with the target protein(s). To investigate the speciation of plecstatin-1 in cell growth media in the presence and absence of foetal bovine serum, and in whole human blood, extended X-ray absorption fine structure spectroscopy data were collected for each of these fluids in the presence of **1**. The data suggest that the arene ring and the bidentate pca ligand remain bound to the Ru ion in all samples, with no ligand dissociation nor dimerisation of the complex observed. The retention of the cym and pca ligands in the Ru complex provides an explanation for the similarity of the metal distributions observed in cells treated with the three complexes – assuming that the Ir and Os complexes are also similarly stable, then the effects of the distinct ligand exchange kinetics of the different metal ions would be masked within the cells. Based on the EXAFS data, it is likely that the labile chlorido ligand of **1**, and by extension **2** and **3**, dissociates in media or blood and is replaced by either a biological thiol or a solvent DMSO molecule. The distinction between this outcome and the observed binding to histidine in protein adducts may reflect the influence of the protein microenvironment on the ligand replacement preference in this class of compounds.

Data availability

The data supporting this article have been included in the ESI.†

Author contributions

J. H. L. conducted all cell culture and sample preparation for both the XFM and XAS experiments, was responsible for all data analysis and preparation of figures and tables, except where noted below. A. T. B. assisted with sample preparation for XAS experiments and was responsible for the human ethics application to collect and experiment with human blood. J. H. L. and H. H. H. collected the XAS and XFM data, conceived the study and wrote the manuscript. B. P. L. configured the beamline at the APS and assisted with XFM data analysis and interpretation. The compounds under study were synthesised by H. O. B. and M. P. S. in the C. G. H. laboratory and C. G. H. edited the manuscript and assisted with conception of the study and interpretation of results. H. O. B. conducted the NMR studies and prepared the relevant figure.

Conflicts of interest

There are no conflicts to declare.

Acknowledgements

H. H. H. acknowledges support from an Australian Research Council Discovery Project (DP210102148). This research used resources of the APS, a U.S. Department of Energy (DOE) Office of Science User Facility operated for the DOE Office of Science by Argonne National Laboratory under contract no. DE-AC02-06CH11357. Part of this research was undertaken on the X-ray Absorption Spectroscopy beamline at the Australian Synchrotron, part of ANSTO. H. O. B. thanks the University of Auckland for a University of Auckland Doctoral Scholarship. We are grateful to Anne Dill for support with the synthesis of plecstatin-1.

References

1 J. P. C. Coverdale, T. Laroiya-McCarron and I. Romero-Canelón, *Inorganics*, 2019, **7**, 31.
2 E. Alessio, G. Balducci, M. Calligaris, G. Costa, W. M. Attia and G. Mestroni, *Inorg. Chem.*, 1991, **30**, 609–618.
3 B. K. Keppler and W. Rupp, *J. Cancer Res. Clin. Oncol.*, 1986, **111**, 166–168.
4 S. M. Meier-Menches, C. Gerner, W. Berger, C. G. Hartinger and B. K. Keppler, *Chem. Soc. Rev.*, 2018, **47**, 909–928.
5 W. D. J. Tremlett, D. M. Goodman, T. R. Steel, S. Kumar, A. Wieczorek-Błauż, F. P. Walsh, M. P. Sullivan, M. Hanif and C. G. Hartinger, *Coord. Chem. Rev.*, 2021, **445**, 213950.
6 P. Zhang and P. J. Sadler, *J. Organomet. Chem.*, 2017, **839**, 5–14.

7 Y. C. Ong and G. Gasser, *Drug Discovery Today: Technol.*, 2020, **37**, 117–124.
8 R. G. Kenny and C. J. Marmion, *Chem. Rev.*, 2019, **119**, 1058–1137.
9 E. Alessio, *Eur. J. Inorg. Chem.*, 2017, **2017**, 1549–1560.
10 E. Alessio and L. Messori, *Molecules*, 2019, **24**, 1995.
11 A. Rilak Simović, R. Masnikosa, I. Bratsos and E. Alessio, *Coord. Chem. Rev.*, 2019, **398**, 113011.
12 J. Arshad, M. Hanif, S. Movassaghi, M. Kubanik, A. Waseem, T. Sohnel, S. M. F. Jamieson and C. G. Hartinger, *J. Inorg. Biochem.*, 2017, **177**, 395–401.
13 J. Arshad, K. K. H. Tong, S. Movassaghi, T. Sohnel, S. M. F. Jamieson, M. Hanif and C. G. Hartinger, *Molecules*, 2021, **26**, 833.
14 C. C. Konkankit, S. C. Marker, K. M. Knopf and J. J. Wilson, *Dalton Trans.*, 2018, **47**, 9934–9974.
15 M. Hanif, M. V. Babak and C. G. Hartinger, *Drug Discovery Today*, 2014, **19**, 1640–1648.
16 S. H. van Rijt, A. F. A. Peacock, R. D. L. Johnstone, S. Parsons and P. J. Sadler, *Inorg. Chem.*, 2009, **48**, 1753–1762.
17 S. Infante-Tadeo, V. Rodríguez-Fanjul, C. C. Vequi-Suplicy and A. M. Pizarro, *Inorg. Chem.*, 2022, **61**, 18970–18978.
18 A. F. A. Peacock, S. Parsons and P. J. Sadler, *J. Am. Chem. Soc.*, 2007, **129**, 3348–3357.
19 A. Gatti, A. Habtemariam, I. Romero-Canelón, J.-I. Song, B. Heer, G. J. Clarkson, D. Rogolino, P. J. Sadler and M. Carcelli, *Organometallics*, 2018, **37**, 891–899.
20 S. J. Dougan and P. J. Sadler, *Chimia*, 2007, **61**, 704.
21 A. L. Noffke, A. Habtemariam, A. M. Pizarro and P. J. Sadler, *Chem. Commun.*, 2012, **48**, 5219–5246.
22 Y. K. Yan, M. Melchart, A. Habtemariam and P. J. Sadler, *Chem. Commun.*, 2005, 4764–4776.
23 S. D. Shnyder, Y. Fu, A. Habtemariam, S. H. van Rijt, P. A. Cooper, P. M. Loadman and P. J. Sadler, *MedChemComm*, 2011, **2**, 666–668.
24 Y. M. Wilson, M. Dürrenberger, E. S. Nogueira and T. R. Ward, *J. Am. Chem. Soc.*, 2014, **136**, 8928–8932.
25 G. Agonigi, T. Riedel, M. P. Gay, L. Biancalana, E. Oñate, P. J. Dyson, G. Pampaloni, E. Păunescu, M. A. Esteruelas and F. Marchetti, *Organometallics*, 2016, **35**, 1046–1056.
26 D. Truong, M. P. Sullivan, K. K. H. Tong, T. R. Steel, A. Prause, J. H. Lovett, J. W. Andersen, S. M. F. Jamieson, H. H. Harris, I. Ott, C. M. Weekley, K. Hummitzsch, T. Söhnel, M. Hanif, N. Metzler-Nolte, D. C. Goldstone and C. G. Hartinger, *Inorg. Chem.*, 2020, **59**, 3281–3289.
27 L. Guo, P. Li, J. Li, Y. Gong, X. Li, Y. Liu, K. Yu and Z. Liu, *Inorg. Chem.*, 2023, **62**, 15118–15137.
28 A. Pastuszko, K. Majchrzak, M. Czyz, B. Kupcewicz and E. Budzisz, *J. Inorg. Biochem.*, 2016, **159**, 133–141.
29 K. J. Kilpin, C. M. Clavel, F. Edafe and P. J. Dyson, *Organometallics*, 2012, **31**, 7031–7039.
30 K. Ghebreyessus, A. Peralta, M. Katdare, K. Prabhakaran and S. Paranawithana, *Inorg. Chim. Acta*, 2015, **434**, 239–251.
31 P. Srivastava, M. Verma, A. Kumar, P. Srivastava, R. Mishra, S. Sivakumar and A. K. Patra, *Dalton Trans.*, 2021, **50**, 3629–3640.
32 R. Fernández, M. Melchart, A. Habtemariam, S. Parsons and P. J. Sadler, *Chem.–Eur. J.*, 2004, **10**, 5173–5179.
33 A. Kurzwernhart, W. Kandioller, É. A. Enyedy, M. Novak, M. A. Jakupec, B. K. Keppler and C. G. Hartinger, *Dalton Trans.*, 2013, **42**, 6193–6202.
34 M. Kubanik, H. Holtkamp, T. Söhnel, S. M. F. Jamieson and C. G. Hartinger, *Organometallics*, 2015, **34**, 5658–5668.
35 A. A. Nazarov, S. M. Meier, O. Zava, Y. N. Nosova, E. R. Milaeva, C. G. Hartinger and P. J. Dyson, *Dalton Trans.*, 2015, **44**, 3614–3623.
36 G. Süss-Fink, *Dalton Trans.*, 2010, **39**, 1673–1688.
37 M. Tomás-Gamasa, M. Martínez-Calvo, J. R. Couceiro and J. L. Mascareñas, *Nat. Commun.*, 2016, **7**, 12538.
38 S. M. Meier, M. Hanif, Z. Adhireksan, V. Pichler, M. Novak, E. Jirkovsky, M. A. Jakupec, V. B. Arion, C. A. Davey, B. K. Keppler and C. G. Hartinger, *Chem. Sci.*, 2013, **4**, 1837–1846.
39 S. M. Meier-Menches, K. Zappe, A. Bileck, D. Kreutz, A. Tahir, M. Cichna-Markl and C. Gerner, *Metallomics*, 2019, **11**, 118–127.
40 S. M. Meier, D. Kreutz, L. Winter, M. H. M. Klose, K. Cseh, T. Weiss, A. Bileck, B. Alte, J. C. Mader, S. Jana, A. Chatterjee, A. Bhattacharyya, M. Hejl, M. A. Jakupec, P. Heffeter, W. Berger, C. G. Hartinger, B. K. Keppler, G. Wiche and C. Gerner, *Angew. Chem., Int. Ed.*, 2017, **56**, 8267–8271.
41 M. H. M. Klose, A. Schoberl, P. Heffeter, W. Berger, C. G. Hartinger, G. Koellensperger, S. M. Meier-Menches and B. K. Keppler, *Monatsh. Chem.*, 2018, **149**, 1719–1726.
42 M. Riisom, L. Eade, W. D. J. Tremlett and C. G. Hartinger, *Metallomics*, 2022, **14**, mfac043.
43 A. F. A. Peacock, A. Habtemariam, S. A. Moggach, A. Prescimone, S. Parsons and P. J. Sadler, *Inorg. Chem.*, 2007, **46**, 4049–4059.
44 P. C. Bruijnincx and P. J. Sadler, *Adv. Inorg. Chem.*, 2009, **61**, 1–62.
45 J. Maksimoska, D. S. Williams, G. E. Atilla-Gokcumen, K. S. Smalley, P. J. Carroll, R. D. Webster, P. Filippakopoulos, S. Knapp, M. Herlyn and E. Meggers, *Chemistry*, 2008, **14**, 4816–4822.
46 B. Boff, C. Gaiddon and M. Pfeffer, *Inorg. Chem.*, 2013, **52**, 2705–2715.
47 N. Pagliaricci, R. Pettinari, F. Marchetti, C. Pettinari, L. Cappellacci, A. Tombesi, M. Cuccioloni, M. Hadiji and P. J. Dyson, *Dalton Trans.*, 2022, **51**, 13311–13321.
48 F. Wang, A. Habtemariam, E. P. van der Geer, R. Fernández, M. Melchart, R. J. Deeth, R. Aird, S. Guichard, F. P. Fabbiani, P. Lozano-Casal, I. D. Oswald, D. I. Jodrell, S. Parsons and P. J. Sadler, *Proc. Natl. Acad. Sci. U. S. A.*, 2005, **102**, 18269–18274.
49 G. E. Büchel, A. Gavriluta, M. Novak, S. M. Meier, M. A. Jakupec, O. Cuzan, C. Turta, J.-B. Tommasino, E. Jeanneau, G. Novitchi, D. Luneau and V. B. Arion, *Inorg. Chem.*, 2013, **52**, 6273–6285.
50 K. J. Franz and N. Metzler-Nolte, *Chem. Rev.*, 2019, **119**, 727–729.
51 K. D. Mjos and C. Orvig, *Chem. Rev.*, 2014, **114**, 4540–4563.

52 A. Casini and A. Pöthig, *ACS Cent. Sci.*, 2024, **10**, 242–250.
53 E. J. Anthony, E. M. Bolitho, H. E. Bridgewater, O. W. L. Carter, J. M. Donnelly, C. Imberti, E. C. Lant, F. Lermyte, R. J. Needham, M. Palau, P. J. Sadler, H. Shi, F.-X. Wang, W.-Y. Zhang and Z. Zhang, *Chem. Sci.*, 2020, **11**, 12888–12917.
54 J. H. Lovett and H. H. Harris, *Curr. Opin. Chem. Biol.*, 2021, **61**, 135–142.
55 M. J. Pushie, I. J. Pickering, M. Korbas, M. J. Hackett and G. N. George, *Chem. Rev.*, 2014, **114**, 8499–8541.
56 E. A. Carter, B. S. Rayner, A. I. McLeod, L. E. Wu, C. P. Marshall, A. Levina, J. B. Aitken, P. K. Witting, B. Lai, Z. Cai, S. Vogt, Y. C. Lee, C. I. Chen, M. J. Tobin, H. H. Harris and P. A. Lay, *Mol. BioSyst.*, 2010, **6**, 1316–1322.
57 K. K. H. Tong, M. Hanif, S. Movassaghi, M. P. Sullivan, J. H. Lovett, K. Hummitzsch, T. Söhnel, S. M. F. Jamieson, S. K. Bhargava, H. H. Harris and C. G. Hartinger, *ChemMedChem*, 2021, **16**, 3017–3026.
58 A. Levina, R. S. Armstrong and P. A. Lay, *Coord. Chem. Rev.*, 2005, **249**, 141–160.
59 R. Ortega, A. Carmona, I. Llorens and P. L. Solari, *J. Anal. At. Spectrom.*, 2012, **27**, 2054–2065.
60 J. J. Woods, J. Lovett, B. Lai, H. H. Harris and J. J. Wilson, *Angew. Chem., Int. Ed.*, 2020, **59**, 6482–6491.
61 J. B. Aitken, S. Antony, C. M. Weekley, B. Lai, L. Spiccia and H. H. Harris, *Metallomics*, 2012, **4**, 1051–1056.
62 C. Sanchez-Cano, D. Gianolio, I. Romero-Canelon, R. Tucoulou and P. J. Sadler, *Chem. Commun.*, 2019, **55**, 7065–7068.
63 Z. Adhireksan, G. E. Davey, P. Campomanes, M. Groessl, C. M. Clavel, H. Yu, A. A. Nazarov, C. H. F. Yeo, W. H. Ang, P. Dröge, U. Rothlisberger, P. J. Dyson and C. A. Davey, *Nat. Commun.*, 2014, **5**, 3462.
64 M. Newville, *Rev. Mineral. Geochem.*, 2014, **78**, 33–74.
65 S. Vogt, *J. Phys. IV France*, 2003, **104**, 635–638.
66 A. L. Ankudinov, B. Ravel, J. J. Rehr and S. D. Conradson, *Phys. Rev. B:Condens. Matter Mater. Phys.*, 1998, **58**, 7565–7576.